nature photonics

Article

https://doi.org/10.1038/s41566-025-01797-9

Spontaneous 2D perovskite formation at the buried interface of perovskite solar cells enhances crystallization uniformity and defect passivation

Received: 27 March 2025

Accepted: 8 October 2025

Yuping Gao[1], Hang Liu[1], Zonglong Song[1], Yu Chen[2], Liu Yang[3], Ziyang Hu[3], Yu Zou[1], Yongsheng Chen[1,4] ✉ & Yongsheng Liu[1,4] ✉

Achieving uniform crystallization across both top and buried interfaces in perovskite films is crucial for unlocking their full photovoltaic potential, yet remains an unresolved challenge. The buried interface, in particular, suffers from poor crystallization relative to the top surface, resulting in suboptimal crystal quality and increased defect densities. Here we propose a one-step strategy to induce the spontaneous formation of near-phase-pure two-dimensional perovskites at the buried interface via the introduction of organic cation halide salts in the perovskite precursor solution. Single-crystal structure analysis highlights the pivotal role of molecular engineering in facilitating the spontaneous formation of buried two-dimensional perovskite phases. The low dipole moments and planar rigidity structures of organic spacers promote their aggregation at perovskite grain boundaries, followed by their migration to the film's bottom interface. The two-dimensional perovskite layer simultaneously promotes uniform crystallization and efficient defect passivation at the buried interface, leading to a power conversion efficiency of 26.31% (certified 26.02%). Unencapsulated devices retain 95% of their initial power conversion efficiency after 1,000 hours of continuous illumination.

Uniform crystallization across perovskite films is crucial for high-performance perovskite solar cells (PSCs). However, the buried interface often exhibits more disordered crystallization and higher defect densities than the top surface[1–3], mainly due to the top-down crystallization process[4,5]. The mismatch in thermal expansion coefficients between the perovskite and the bottom layer induces substantial residual strain at the buried interface, further contributing to defect formation and non-radiative recombination[2,6]. This interfacial disparity often leads to non-uniform film properties, hindering charge transport and device stability. Although the buried interface critically impacts device performance[7], most crystallization control strategies predominantly focused on the bulk phase[8–11], with relatively few studies addressing the challenge of enhancing crystal uniformity between the top and bottom surfaces. Achieving both uniform film crystallization and effective defect passivation of the buried interface remains challenging, requiring more advanced and integrated approaches[12,13]. Compounding this issue is the tendency of the spin-coated interfacial layer to exhibit weak adhesion to the substrate, making it prone to

---

[1]State Key Laboratory of Elemento-Organic Chemistry, the Centre of Nanoscale Science Technology and Key Laboratory of Functional Polymer Materials, Frontiers Science Center for New Organic Matter, College of Chemistry, Nankai University, Tianjin, China. [2]Institute of High Energy Physics, Chinese Academy of Sciences, Beijing, China. [3]Department of Microelectronic Science and Engineering, Ningbo University, Ningbo, China. [4]Haihe Laboratory of Sustainable Chemical Transformations, Tianjin, China. ✉e-mail: yschen99@nankai.edu.cn; liuys@nankai.edu.cn

being washed away or absorbed into the perovskite bulk during film formation[1,12,14,15], which compromises its defects passivation efficiency. Therefore, strategies that simultaneously regulate film uniformity and stabilize the buried interface are critical for further improving the performance of PSCs.

Two-dimensional (2D) perovskites can template the oriented crystallization of α-$FAPbI_3$ and regulate the crystallization dynamics[11,16]. They can also act as an effective passivation layer, improving defect suppression, stability and energy alignment, ultimately leading to more efficient and durable devices[17–20]. The 2D perovskites or organic spacers are typically added into the perovskite precursor solution, followed by spin coating an additional 2D perovskite layer to fabricate high-performance PSCs[8,9,21]. However, this approach primarily regulates bulk crystallization, as the incorporated 2D perovskite phase tends to remain within the bulk rather than at the buried interface. Additionally, 2D perovskite passivation techniques are typically effective for the top surface, and extending it to the buried interface within PSCs presents substantial challenges[12,13]. Preforming a 2D perovskite layer on the substrate offers a potential route to construct a buried 2D phase and regulate three-dimensional (3D) film growth. Such a layer has been demonstrated to contribute to the control of perovskite crystallization[14]. However, this regulation occurred due to the dissolution of the 2D phase back into the perovskite precursor solution. Constructing a stable buried 2D perovskite phase to induce the growth of a high-quality 3D perovskite presents a critical challenge, as these layers are often washed away or disrupted during film formation.

In this work, we demonstrated an effective strategy for fabricating high-quality 2D/3D perovskite films through the spontaneous formation of a near-phase-pure 2D perovskite layer at the buried interfaces. This layer not only passivates the buried interfacial defects but also enhances crystal uniformity across the film. Specifically, we incorporated either 2,3-dihydroisoindole hydroiodide (DHIII) or 4,5,6,7-tetra hydrothieno[3,2-*c*]pyridine hydroiodide (ThPyI) into the perovskite precursor solution. During annealing, these organic cations migrated downwards with top-down crystallization and formed a 2D perovskite at the buried interface, improving crystallization quality across the film. It is found that the unique properties of DHII and ThPy spacers stem from their low dipole moments and planar rigid structures. Their small dipole moments minimized lattice interactions, whereas their rigid aromatic structures enhanced intermolecular non-covalent interactions and promoted aggregation. These characteristics facilitated their downward migration, regulating both buried interface orientation and crystallization kinetics. As a result, this two-birds-with-one-stone strategy resulted in remarkable improvements in power conversion efficiency (PCE), reaching up to 26.31% (certified 26.02%), along with greatly enhanced stability. Importantly, the buried 2D perovskite layer can be realized via both one-step and two-step spin-coating methods, and is compatible with diverse perovskite compositions (bandgaps of 1.55 eV and 1.70 eV).

Results and discussion

Non-uniformity between top and bottom surfaces

We fabricated $FA_{1-x}Cs_xPbI_3$ ($x = 0.02$) perovskite films (control films) and compared their top and bottom interfaces. An ultraviolet-curable adhesive was used to peel off the film from the ITO/SnO_2 substrate, exposing the perovskite bottom surface and the SnO_2 top surface[22] (Fig. 1a and Supplementary Fig. 1). The field-emission scanning electron microscopy (SEM) images revealed that the top surface exhibited considerably larger grains than the bottom interface (Fig. 1b), indicating non-uniform film crystallization. Grazing-incidence X-ray diffraction (GIXRD) at 1.0° incidence revealed weaker and shifted diffraction peaks at the buried interface compared with the top surface, confirming markedly inferior crystallinity near the bottom interface (Fig. 1c). Grazing-incidence wide-angle X-ray scattering (GIWAXS) showed a pronounced difference in orientation distribution, with the top surface peaking at 0° and the bottom at ~52° (Fig. 1d and Supplementary Fig. 2), indicating less-controlled crystallization and probably higher defects near the substrate. The photoluminescence (PL) spectra further confirmed that the buried interface showed markedly weaker emission at ~790 nm. This difference persists even though the buried interface measurements were taken through the glass, an arrangement that normally enhances both excitation and emission, indicating a higher density of defects and non-radiative recombination losses at the buried interface[23–25] (Fig. 1e). Time-resolved photoluminescence (TRPL) measurements also revealed shorter carrier lifetimes at the bottom interface (Fig. 1f).

The buried interface of the perovskite films typical exhibits inferior crystallization compared with the top surface due to the substrate-induced disruption of nucleation and growth[1,2], which introduces strain and smaller grains, and higher defect densities. Although the exposed top surface benefits from Ostwald ripening during annealing[26,27], space constraints at the buried interface suppress this process, further limiting grain growth and increasing defects, resulting in non-uniform film properties.

Improving non-uniformity through buried 2D perovskites

To improve crystallization uniformity across the top and buried interfaces, a 2D/3D heterojunction strategy at the buried interface was developed. 2D perovskites can regulate film crystallization[11,21] and passivate the interface defects[19,28]. However, preforming them on substrates is impractical due to solvent dissolution and limited control over crystallization[12,14] (Supplementary Fig. 3 and Supplementary Note 2). Moreover, due to the top-down crystallization process, buried interface treatments often fail to control the perovskite crystallization rate and orientation. A more effective approach is to introduce organic spacers into the precursor solution, enabling them to migrate downwards during crystallization. This synchronized process regulates the film quality at different depths, whereas the spacers accumulate at the buried interface to form 2D perovskite phases that control orientation and passivate defects. However, achieving this goal is challenging and requires precise molecular design.

The molecular structure design of organic spacers was illustrated in Fig. 1g. Compared with the conventional primary ammonium spacers, such as phenethlyammonium (PEA) and 2-thiophenemethylammonium (ThMA), secondary ammonium spacers DHII and ThPy exhibit increased rigidity and markedly reduced dipole moments. Accordingly, DHIII and ThPyI, along with the control organic cation halides phenethlyammonium iodide (PEAI) and ThMAI, were used to fabricate 2D/3D hybrid perovskite films (Fig. 1h). Both DHIII and ThPyI induced the spontaneous formation of 2D perovskite layers at the buried interface, whereas PEAI and ThMAI failed to do so (Fig. 1i and Supplementary Fig. 4). In ThPyI-based films, the buried interface exhibited a gradient-ordered 2D perovskite distribution, with $n = 2$ phases concentrated deepest and $n = 3$ phases enriched towards the top layers (Supplementary Note 3). By contrast, the buried surface and SnO_2 surface of the DHIII-based film exhibited PL features dominated by the $n = 2$ phase with minimal contributions from higher-n phases (Supplementary Fig. 5c), indicating a near-phase-pure 2D perovskite.

We subsequently peeled off the perovskite film containing near-phase-pure buried 2D perovskites (target perovksites) and studied the crystallization quality of both top and buried interfaces. SEM and GIXRD revealed nearly identical diffraction patterns and enlarged grain size (~1 μm) at both interfaces (Fig. 2a,b), unlike the control film (Fig. 1c), demonstrating enhanced crystallization uniformity across the entire film. The buried interface also exhibited higher hydrophobicity, consistent with 2D phase formation (Fig. 2c). The enhanced film quality at the buried interface also resulted in improved crystallization orientation, aligning both the top and bottom layers in a preferred out-of-plane orientation, favouring vertical carrier transport[8,11] (Fig. 2d,e and Supplementary Fig. 2), whereas compressive strain at the buried interface was largely suppressed (Fig. 2f). GIXRD measurements

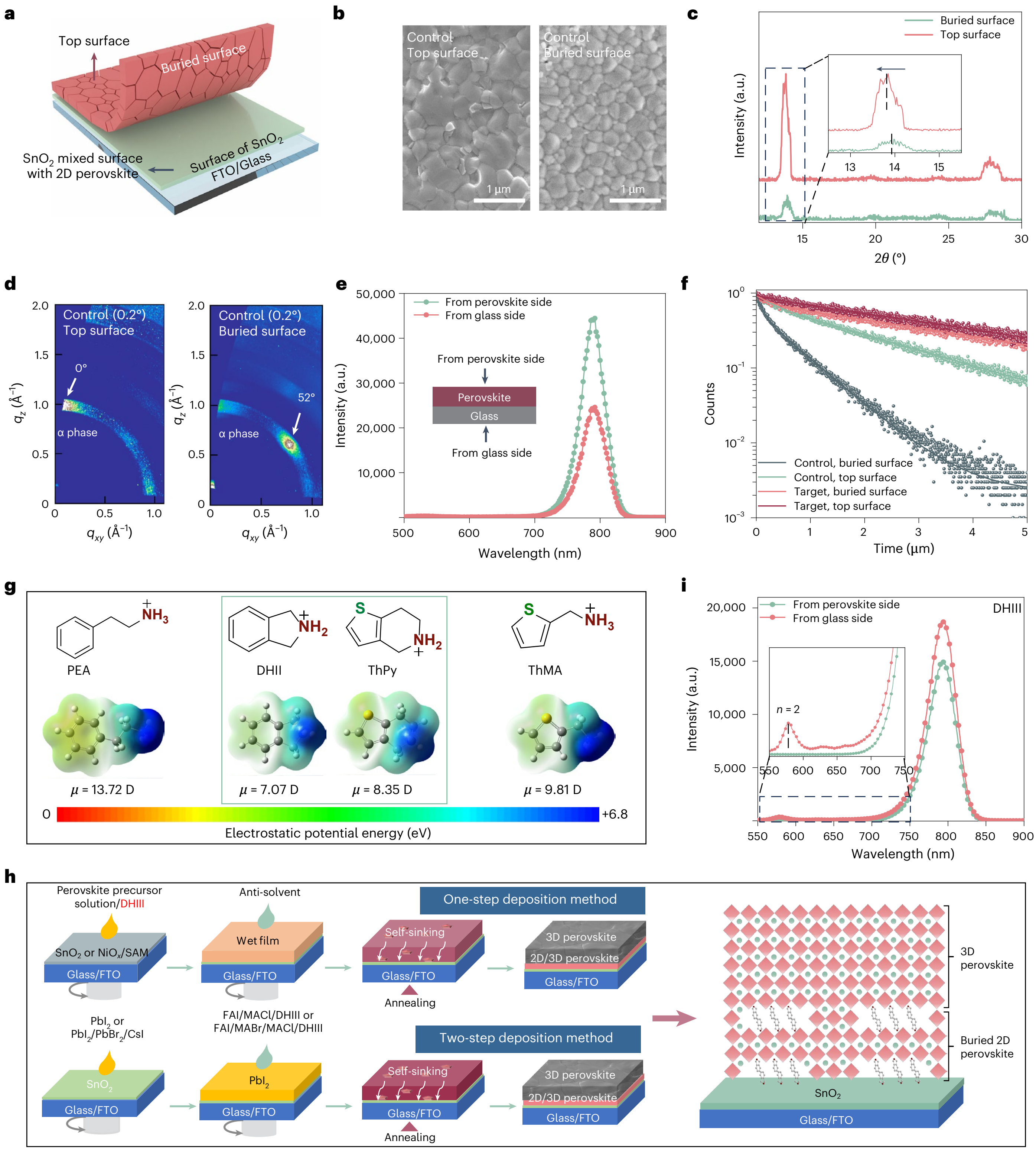

Fig. 1 | Morphology of top and bottom surfaces. a, Schematic of peeling off the buried interface from the device. **b**, Top-view and bottom-view SEM images of the control perovskite films. **c**, GIXRD patterns of the control perovskite films on glass/SnO_2 substrates, measured from the top and detached buried surfaces. **d**, 2D GIWAXS images of the control perovskite films on glass/SnO_2 substrates, measured from the top and detached buried surfaces. The grazing-incidence angle was 0.2°. **e**, PL spectra of the control perovskite films obtained from different incident directions. **f**, TRPL spectra of the perovskite films obtained from different incident directions. **g**, Chemical structures and electrostatic potential map of organic spacers. **h**, Schematic of the 2D/3D perovskite formation at the buried interface via both one-step and two-step spin-coating methods. **i**, PL spectra of the 2D/3D perovskite films obtained from different incident directions.

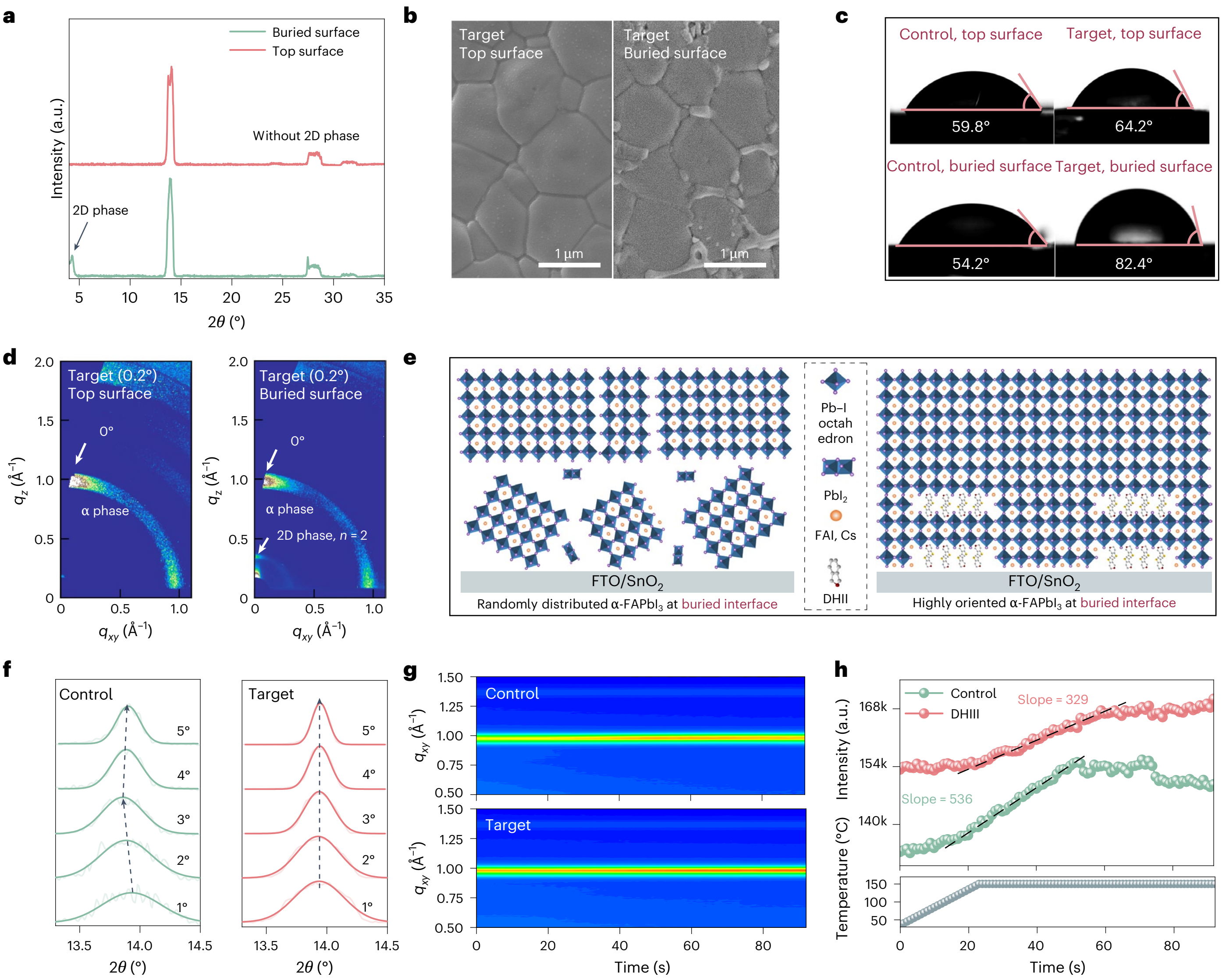

Fig. 2 | Improving non-uniformity via buried 2D perovskites. **a**, GIXRD patterns of the 2D/3D perovskite films measured from the top and bottom surfaces. **b**, Top-view and bottom-view SEM images of the 2D/3D perovskite films. **c**, Contact angles of water on the perovskite film surface. **d**, 2D GIWAXS images of the target perovskite films measured from the top and buried surfaces. The grazing-incidence angle was 0.2°. **e**, Schematic of the oriented crystallization of the perovskite film at the buried interface facilitated by 2D perovskite phases. **f**, GIXRD patterns for the control and target perovskite films measured at the bottom interface. **g**, Structural evolution monitored by azimuthally integrated in situ GIWAXS of the as-deposited films during annealing. **h**, Integrated intensity of α-$FAPbI_3$ during the annealing process extracted from 2D GIWAXS over time. Temperature ramped from room temperature to 150 °C at ~5 °C s^{-1}.

at the buried interface showed that the diffraction peaks of the control films gradually shifted to lower angles as the incident angle increased from 1.0° to 3.0°, but remained largely unchanged at 5°, indicating that compressive strain concentrated near the substrate. By contrast, the diffraction peaks of the target perovskite film remained stable throughout. This reduced strain originates from the buried-DHIII-induced near-phase-pure 2D perovskite layer, which lattice matches with the overlying 3D phase to buffer thermal-mismatch-induced strain (Supplementary Fig. 7a) and simultaneously slows crystallization, enabling larger, defect-minimized grains.

Compared with the control film, the introduction of the buried 2D perovskite phase markedly improved film uniformity and overall crystallization quality, yielding larger grains and stronger X-ray diffraction peaks (Supplementary Fig. 5d). In situ GIWAXS analysis showed that DHIII slowed crystallization, reducing the crystallization slope from 536 to 329 (refs. 11,29) (Fig. 2g,h), thereby suppressing rapid α-$FAPbI_3$-rich crystal growth and enabling more uniform, defect-minimized grain formation. In particular, the control films showed post-peak intensity decay due to humidity-induced degradation during thermal annealing, absent in a DHIII-based film. In particular, PL and TRPL measurements with different charge transport layer stacks (Supplementary Fig. 9 and Supplementary Note 5) showed that DHIII enhances both bulk and buried interface quality, increasing carrier lifetimes and reducing non-radiative recombination[30]. The PL intensity and PL lifetime at the buried interface of the target perovskite film were nearly identical to those at the top surface, confirming this conclusion (Fig. 1f,i). By contrast, PEAI- and ThMAI-based films showed large interfacial disparity (Supplementary Fig. 4). These results highlight the templating role of the spontaneously formed $n = 2$ buried 2D phase, which modulates the nucleation kinetics by slowing down early stage crystallization, promotes vertical grain orientation (in situ GIWAXS measurements) and improves film morphology and crystallinity, ultimately benefiting device performance.

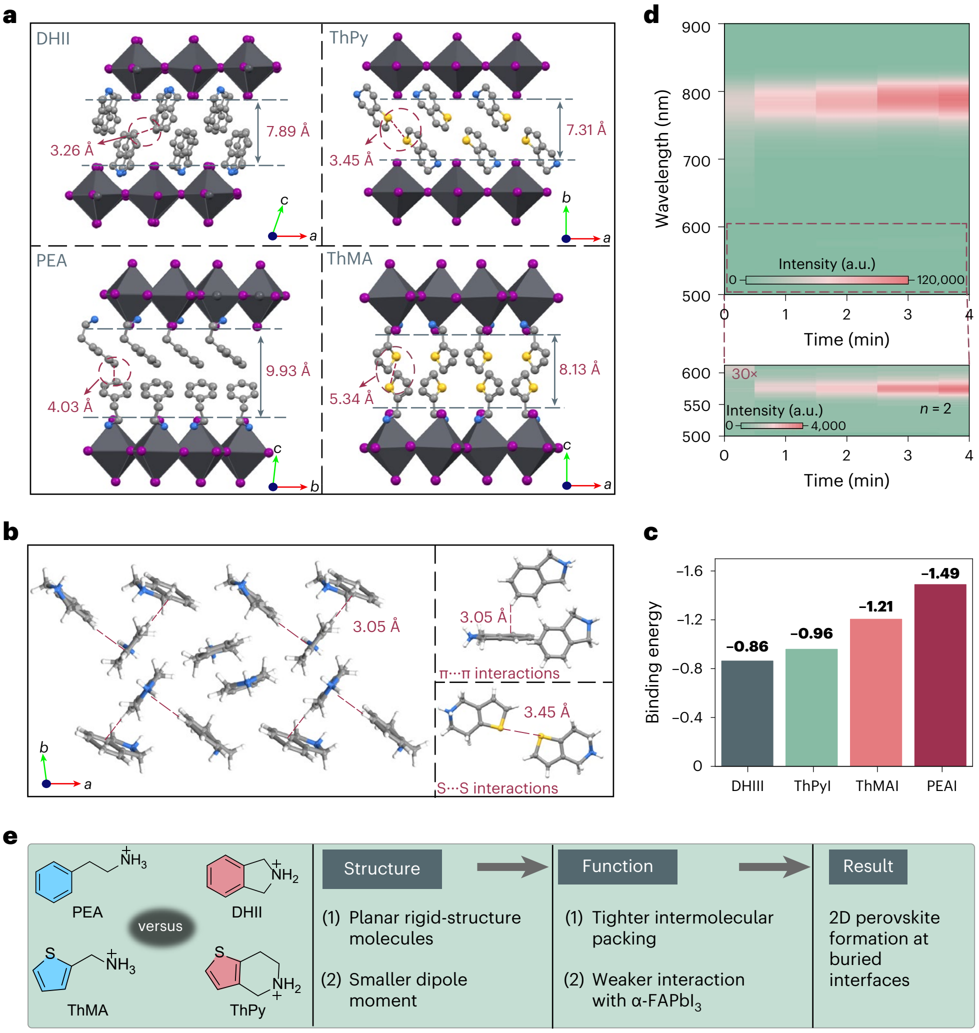

Fig. 3 | Mechanism of spontaneous 2D perovskite formation at the buried interface. a, Single-crystal structure of the 2D perovskites. **b**, Arrangement of DHII and ThPy within the perovskite lattices, with inorganic layers omitted for the sake of clarity. The dashed line indicates non-covalent interactions. **c**, Binding energy of the organic spacers absorbed on the $FAPbI_3$ crystal surface. **d**, Heat map of semi-in situ PL spectra of perovskite films incorporating an organic spacer during the annealing process. The sample structure was glass/perovskite, and the PL measurements were performed from the glass side. **e**, Structure–function result relationship analysis of the four 2D spacers for perovskite films.

Mechanism of spontaneous formation of buried 2D perovskites

To elucidate the formation mechanism of buried 2D perovskites, we compared the single-crystal structures of the 2D perovskite based on the four organic spacers. $(DHII)_2PbI_4$ and $(ThPy)_2PbI_4$ exhibited much shorter interlayer spacings (7.89 Å and 7.31 Å, respectively) compared with $(PEA)_2PbI_4$ and $(ThMA)_2PbI_4$ (9.93 Å and 8.13 Å, respectively), indicating tighter packing (Fig. 3a). In $(DHII)_2PbI_4$, adjacent DHII spacers were separated by only 3.26 Å, below the van der Waals distance, with additional edge-tilted T-shaped π–π interactions[31] (Fig. 3b and Supplementary Fig. 10). Similarly, $(ThPy)_2PbI_4$ showed 3.45 Å S···S contacts[32], whereas such non-covalent interactions were absent in the PEA- and ThMA-based 2D perovskites (Supplementary Fig. 11). These observations confer the more rigid structure of DHII and ThPy spacers, resulting in a greater tendency for molecular aggregation. The solubility experiments showed that PEAI and ThMAI dissolved >100 mg ml^{-1} in isopropanol (IPA), whereas ThPyI and DHIII dissolved <10 mg ml^{-1} (Supplementary Fig. 12). The resulting aggregates of organic spacers have a larger volume and mass, making them more prone to being extruded to the bottom surface of the film during top-down crystallization[33]. Moreover, the smaller van der Waals gaps in DHII- and ThPy-based 2D perovskites contribute to enhanced structural stability[34], whereas additional π–π interactions inhibit organic cation diffusion, reinforcing structural cohesion[28]. Unlike typical strong spacer aggregation that destabilizes 2D perovskites into 1D/0D phases[28,35], the rational molecular design of DHIII and ThPyI balances intermolecular interactions with structural stability, enabling a robust buried 2D layer. Theoretical calculations revealed weaker binding energies of DHII (−0.86 eV) and ThPy (−0.96 eV) with $FAPbI_3$ compared with PEA and ThMA (Fig. 3c), consistent with their rigid structures and lower dipole moments. It was also confirmed by ^1H nuclear magnetic resonance, where amine protons in PEA and ThMA shifted to a higher field after PbI_2 addition, whereas DHII and ThPy showed no shift (Supplementary Fig. 14). Consequently, PEAI and ThMA remain trapped in the bulk of the perovskite film[36,37], whereas DHIII and ThPyI migrate to the buried interface. Semi-in situ PL measurements confirmed the concurrent formation of buried 2D perovskite with $FAPbI_3$-rich perovskite crystallization (Fig. 3d), supporting this extrusion mechanism. The design principles and structure–function correlation of the spacers are summarized in Fig. 3e.

Device performance and stability

Here n–i–p-type devices were fabricated to evaluate the effect of the buried 2D perovskite layer on photovoltaic performance. As shown in Supplementary Fig. 17a, ThPyI- and DHIII-based devices

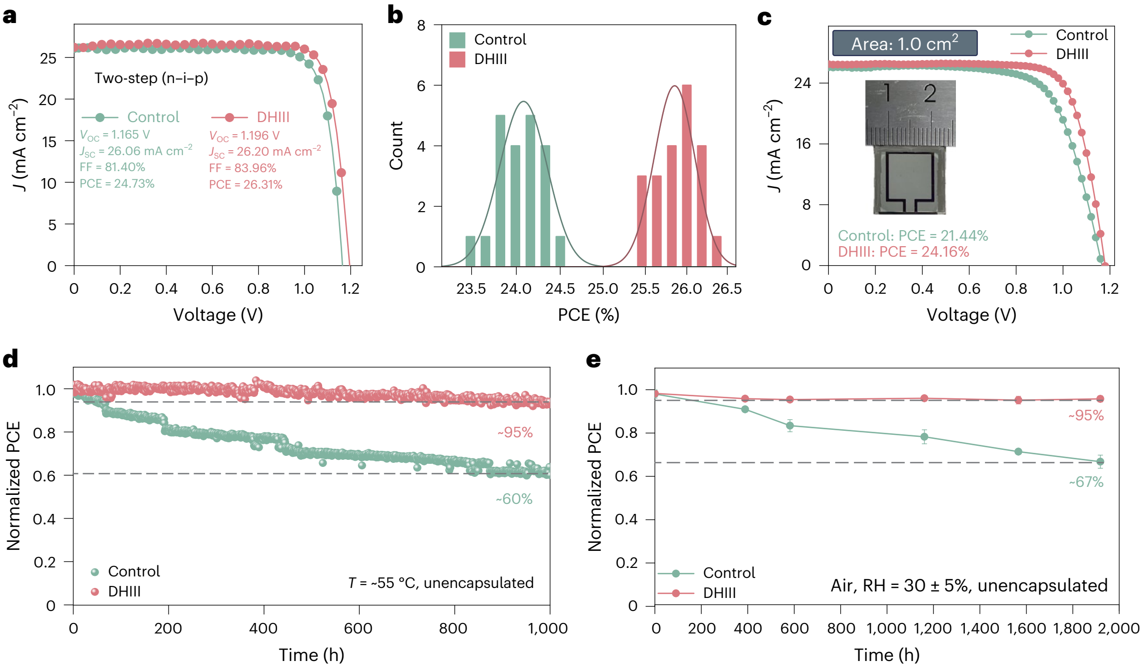

Fig. 4 | Device performance and stability. **a**, J–V curves of the best-performing control and DHIII-based devices fabricated using two-step deposition method. **b**, PCE distributions of the control and DHIII-based PSC devices. **c**, J–V curve of the devices with area of 1.0 cm^2. **d**, Evolution of normalized PCE of the unencapsulated device with time under light-emitting diode illumination (100 mW cm^{-2}) in a nitrogen-filled glovebox. **e**, Normalized PCEs versus time for unencapsulated devices stored in ambient condition (room temperature; relative humidity (RH), 35 ± 5%). Data from the three cells are collected and presented as mean ± s.e.m.

demonstrated substantially improved average PCE of 25.16% and 25.73%, respectively, compared with 23.86% for the controls. The enhanced efficiency could be attributed to reduced interfacial defects and suppressed non-radiative recombination, yielding improved open-circuit voltage (V_{OC}) and fill factor (FF; Supplementary Fig. 17b). Light-intensity-dependent V_{OC} measurement confirmed lower recombination in DHIII-based devices (Supplementary Fig. 17c). DHIII also induced a slight short-circuit current density (J_{SC}) increase due to a narrowed bandgap and strain relaxation effects (Supplementary Fig. 17d–f). The in situ formation of a buried 2D perovskite layer templates the growth of larger, better-ordered $FAPbI_3$-rich grains with reduced defectivity, which can modestly alter the intrinsic optical bandgap. In particular, the average PCE of the ThPyI-based system, featuring a multi-n-value 2D perovskite phase, was slightly lower than that of the DHIII-based system. Although the ThPyI system demonstrated a gradient-ordered 2D perovskite structure with multiple n values, this phase gradient was essentially a macroscopic average. At the nanoscale, however, a disordered phase arrangement persisted[38,39], potentially leading to multiple quantum wells that inevitably trapped charge carriers and hindered charge transport[40,41]. By contrast, the near-phase-pure 2D perovskite based on DHIII at the buried interface effectively passivates defects and greatly minimizes recombination[12,19,42]. Thus, the following sections focus on the DHIII system.

Figure 4a presented the current density–voltage (J–V) curves of the best-performing control and DHIII-based devices measured under standard AM1.5G light illumination (100 mW cm^{-2}). The control device achieved the best PCE of 24.73%, with a V_{OC} of 1.165 V and an FF of 81.40%. On self-forming a 2D perovskite layer at the buried interface, the DHIII-treated device shows a V_{OC} of 1.196 V and an FF of 83.96%, yielding an impressive PCE of 26.31%. The certified PCE is 26.02% (Supplementary Fig. 22), which is among the highest for conventional n–i–p PSCs. Statistical analysis confirmed excellent reproducibility (Fig. 4b), underscoring the effectiveness of the 2D perovskite passivation in boosting device efficiency. Time-of-flight secondary ion mass spectrometry (ToF-SIMS) depth profiling results confirmed the consistent interfacial localization of DHII across multiple batches (Supplementary Fig. 25a–c), and statistical analysis of device performance demonstrated high reproducibility in key photovoltaic parameters (Supplementary Fig. 25d,e), thereby supporting the robustness of the spontaneous formation of the buried 2D perovskite phase. Devices with larger areas (1.0 cm^2) also benefited, with PCE increasing form 21.44% (control) to 24.12% (Fig. 4c). In particular, the formation of the buried 2D perovskite is not limited to two-step deposition. Introducing DHIII directly into a one-step precursor still produced a phase-pure $n = 2$ layer at the bottom interface (Supplementary Fig. 26a), and the effect also extended to wide-bandgap compositions ($E_g = 1.70$ eV; Supplementary Fig. 26b). Preliminary device results show that DHIII increases the PCE of one-step n–i–p devices from 22.46% to 24.15%, and p–i–n devices from 24.74% to 25.94% based on 1.55-eV-bandgap films (Supplementary Fig. 27). Ultraviolet photoelectron spectroscopy analysis revealed a deeper valence band maximum and larger work function for the buried 2D phase based on DHIII compared with the 3D perovskite, explaining the architecture-independent performance improvement[12] (Supplementary Fig. 28 and Supplementary Note 10). Wide-bandgap ($E_g = 1.70$ eV) devices fabricated via the two-step process also improved from 18.50% to 20.95% on DHIII incorporation (Supplementary Fig. 29). These results indicate that the performance enhancement is intrinsic to the spacer, independent of the deposition protocol or bandgap.

To assess the long-term stability, unencapsulated devices underwent maximum power-point (MPP) tracking under continuous light illumination (100 ± 10 mW cm^{-2}, white light-emitting diode) in N_2 (T = ~55 °C). As shown in Fig. 4d, the DHIII-based device demonstrated greatly improved operational stability, maintaining 95% of its initial PCE after 1,000 h, compared with only 60% for the control. To ensure statistical robustness, we performed two additional MPP tests (635 h each) alongside the original 1,000-h trace (Supplementary Fig. 30a–d). From these, we extracted PCE_{MPP}

at 50-h intervals and performed statistical analysis. As shown in Supplementary Fig. 30e, DHIII-treated cells preserved 98% of their initial efficiency at 635 h, whereas the control device dropped to 70%. Parameter decomposition revealed that FF_{MPP} in the control devices falls to 75% of its initial value (Supplementary Fig. 30f), whereas $V_{OC,MPP}$ declined to 95% (Supplementary Fig. 30g) and $J_{SC,MPP}$ remained unchanged (Supplementary Fig. 30h). By contrast, DHIII-based devices exhibited only a minor FF reduction (~3%), with negligible changes in the other parameters. During MPP tracking, the dominant performance losses, therefore, occur in V_{OC} and FF, whereas J_{SC} remains essentially unchanged. Such a degradation signature has previously been linked to defect formation at the perovskite–HTL interface, which promotes non-radiative recombination (reducing V_{OC}) and increases series/contact resistance (reducing FF) but minimally affects J_{SC}[43,44]. Potential contributions from bulk processes, such as ion migration, are also discussed in Supplementary Note 11. Ambient stability tests at 35% relative humidity revealed that the unencapsulated DHIII-based devices retained 95% of their initial PCE after ~2,000 h of storage (Fig. 4e). This improved durability can be attributed to the spontaneous formation of a buried 2D perovskite layer, which passivates traps, improves crystallinity, suppresses moisture diffusion and synergizes with top-surface treatments to create a dual-barrier system. Hence, in addition to PCE enhancement, the buried 2D perovskite layer markedly improves both operational and ambient stability in PSCs.

Discussion

We have developed a one-step strategy that enables the spontaneous formation of near-phase-pure 2D perovskites at the buried interfaces, achieving both crystallization uniformity and defect passivation, driven by the molecular design of organic spacers. Compared with ThMA and PEA spacers, DHII and ThPy exhibited lower dipole moments and more planar rigid structures. These features promote stronger molecular stacking and weaker interactions with $FAPbI_3$-rich perovskite, enabling their extrusion to the film bottom during the top-down crystallization process. This molecular sinking regulates crystallization dynamics, optimizes crystal orientation and minimizes interfacial non-radiative recombination, leading to remarkable improvements in both photovoltaic performance and stability. This work underscores the critical role of molecular design in controlling the buried 2D perovskite distribution, regulating crystallization dynamics and optimizing the crystal orientation, thereby offering a promising pathway for advancing PSCs.

Online content

Any methods, additional references, Nature Portfolio reporting summaries, source data, extended data, supplementary information, acknowledgements, peer review information; details of author contributions and competing interests; and statements of data and code availability are available at https://doi.org/10.1038/s41566-025-01797-9.

References

1. Min, H. et al. Perovskite solar cells with atomically coherent interlayers on SnO_2 electrodes. *Nature* **598**, 444–450 (2021).
2. Luo, C. et al. Engineering the buried interface in perovskite solar cells via lattice-matched electron transport layer. *Nat. Photon.* **35**, 2303139 (2023).
3. Wang, F. et al. Two-step perovskite solar cells with >25% efficiency: unveiling the hidden bottom surface of perovskite layer. *Adv. Mater.* **36**, 2401476 (2024).
4. Chen, S. et al. Stabilizing perovskite-substrate interfaces for high-performance perovskite modules. *Science* **373**, 902–907 (2021).
5. Chen, S. et al. Crystallization in one-step solution deposition of perovskite films: upward or downward? *Sci. Adv.* **7**, eabb2412 (2021).
6. Liu, S. et al. Buried interface molecular hybrid for inverted perovskite solar cells. *Nature* **632**, 536–542 (2024).
7. Xiao, Y., Yang, X., Zhu, R. & Snaith, H. J. Unlocking interfaces in photovoltaics. *Science* **384**, 846–848 (2024).
8. Shi, P. J. et al. Oriented nucleation in formamidinium perovskite for photovoltaics. *Nature* **620**, 323–327 (2023).
9. Park, J. et al. Controlled growth of perovskite layers with volatile alkylammonium chlorides. *Nature* **616**, 724–730 (2023).
10. Huang, Z. et al. Anion-π interactions suppress phase impurities in $FAPbI_3$ solar cells. *Nature* **623**, 531–537 (2023).
11. Gao, Y. et al. Controlled nucleation and oriented crystallization of methylammonium-free perovskites via in situ generated 2D perovskite phases. *Adv. Mater.* **36**, 2405921 (2024).
12. Azmi, R. et al. Double-side 2-dimensional/3-dimensional heterojunctions for inverted perovskite solar cells. *Nature* **628**, 93–98 (2024).
13. Li, H. Y. et al. 2D/3D heterojunction engineering at the buried interface towards high-performance inverted methylammonium-free perovskite solar cells. *Nat. Energy* **8**, 946–955 (2023).
14. Wang, Y. et al. Highly oriented $FAPbI_3$ via 2D Ruddlesden Popper perovskite template growth. *Adv. Energy Mater.* **14**, 2401721 (2024).
15. Li, Q. et al. Harmonizing the bilateral bond strength of the interfacial molecule in perovskite solar cells. *Nat. Energy* **9**, 1506–1516 (2024).
16. Song, S. et al. Molecular engineering of organic spacer cations for efficient and stable formamidinium perovskite solar cell. *Adv. Energy Mater.* **10**, 2001759 (2020).
17. Park, S. M. et al. Engineering ligand reactivity enables high-temperature operation of stable perovskite solar cells. *Science* **381**, 209–215 (2023).
18. Azmi, R. et al. Damp heat-stable perovskite solar cells with tailored-dimensionality 2D/3D heterojunctions. *Science* **376**, 73–77 (2022).
19. Sidhik, S. et al. Deterministic fabrication of 3D/2D perovskite bilayer stacks for durable and efficient solar cells. *Science* **377**, 1425–1430 (2022).
20. Wang, J. et al. Bilayer interface engineering through 2D/3D perovskite and surface dipole for inverted perovskite solar modules. *eScience* **4**, 100308 (2024).
21. Zhou, T. et al. Crystal growth regulation of 2D/3D perovskite films for solar cells with both high efficiency and stability. *Adv. Mater.* **34**, 2200705 (2022).
22. Zhang, C. et al. Work function tuning of a weak adhesion homojunction for stable perovskite solar cells. *Joule* **8**, 1394–1411 (2024).
23. Cho, H. et al. Overcoming the electroluminescence efficiency limitations of perovskite light-emitting diodes. *Science* **350**, 1222–1225 (2015).
24. Zhao, Y. et al. Inactive $(PbI_2)_2RbCl$ stabilizes perovskite films for efficient solar cells. *Science* **377**, 531–534 (2022).
25. Gao, H. et al. Homogeneous crystallization and buried interface passivation for perovskite tandem solar modules. *Science* **383**, 855–859 (2024).
26. Meng, R. et al. Solvent bath annealing-induced liquid phase Ostwald ripening enabling efficient and stable perovskite solar cells. *J. Mater. Chem. A* **11**, 4780–4788 (2023).
27. Li, N. et al. Liquid medium annealing for fabricating durable perovskite solar cells with improved reproducibility. *Science* **373**, 561–567 (2021).
28. Liu, C. et al. Two-dimensional perovskitoids enhance stability in perovskite solar cells. *Nature* **633**, 359–364 (2024).
29. Zhang, K. et al. Highly efficient and stable $FAPbI_3$ perovskite solar cells and modules based on exposure of the (011) facet. *Nano-Micro Lett.* **15**, 138 (2023).

30. Krogmeier, B., Staub, F., Grabowski, D., Rau, U. & Kirchartz, T. Quantitative analysis of the transient photoluminescence of $CH_3NH_3PbI_3/PC_{61}BM$ heterojunctions by numerical simulations. *Sustain. Energy Fuels* **2**, 1027–1034 (2018).
31. Jennings, W. B., Farrell, B. M. & Malone, J. F. Attractive intramolecular edge-to-face aromatic interactions in flexible organic molecules. *Acc. Chem. Res.* **34**, 885–894 (2001).
32. Bai, M. et al. A donor-acceptor-donor structured organic conductor with S···S chalcogen bonding. *Cryst. Growth Des.* **14**, 459–466 (2014).
33. Tan, Q. et al. Inverted perovskite solar cells using dimethylacridine-based dopants. *Nature* **620**, 545–551 (2023).
34. Shao, J.-Y. et al. Recent progress in perovskite solar cells: material science. *Sci. China Chem.* **66**, 10–64 (2022).
35. Liu, Y., Guo, J., Zhou, H., Li, C. & Guo, X. Correlating π-π stacking of aromatic diammoniums with stability and dimensional reduction of Dion-Jacobson 2D perovskites. *J. Am. Chem. Soc.* **146**, 8198–8205 (2024).
36. Lee, J. W. et al. 2D perovskite stabilized phase-pure formamidinium perovskite solar cells. *Nat. Commun.* **9**, 3021 (2018).
37. Zhou, T. et al. Highly efficient and stable solar cells based on crystalline oriented 2D/3D hybrid perovskite. *Adv. Mater.* **31**, 1901242 (2019).
38. Lin, Y. et al. Unveiling the operation mechanism of layered perovskite solar cells. *Nat. Commun.* **10**, 1008 (2019).
39. Hoffman, J. M. et al. Film formation mechanisms in mixed-dimensional 2D/3D halide perovskite films revealed by in situ grazing-incidence wide-angle X-ray scattering. *Chem* **8**, 1067–1082 (2022).
40. Quintero-Bermudez, R. et al. Ligand-induced surface charge density modulation generates local type-II band alignment in reduced-dimensional perovskites. *J. Am. Chem. Soc.* **141**, 13459–13467 (2019).
41. Yu, D. et al. Direct observation of photoinduced carrier blocking in mixed-dimensional 2D/3D perovskites and the origin. *Nat. Commun.* **13**, 6229 (2022).
42. Jang, Y.-W. et al. Intact 2D/3D halide junction perovskite solar cells via solid-phase in-plane growth. *Nat. Energy* **6**, 63–71 (2021).
43. Julien, A., Puel, J.-B. & Guillemoles, J.-F. Distinction of mechanisms causing experimental degradation of perovskite solar cells by simulating associated pathways. *Energy Environ. Sci.* **16**, 190–200 (2023).
44. Zhao, B. X. et al. A hole-transport material that also passivates perovskite surface defects for solar cells with improved efficiency and stability. *Energy Environ. Sci.* **13**, 4334–4343 (2020).

Methods

Materials

We used SnO_2 colloid precursor (tin(IV) oxide, 15% in H_2O colloidal dispersion, Alfa Aesar), *N*,*N*-dimethylformamide (DMF; 99.8%, J&K Scientific), dimethyl sulfoxide (DMSO; 99.9%, J&K Scientific), IPA (Shanghai Aladdin Biochemical Technology), chlorobenzene (CB; 99.5% and 99.9%, J&K Scientific), PbI_2 (99.99%, TCI, purchased from J&K Scientific), caesium iodide (CsI; 99.999%, Advanced Election Technology), 2,2′,7,7′-tetrakis[*N*,*N*-di(4-methoxyphenyl)amino]-9,9′-spiro-bifluorene (Spiro-OMeTAD; Advanced Election Technology), HI aqueous solution (55%–57% w/w, Adamas), 4-*tert*-butylpyridine (99.9%, Alfa Aesar), lithium bis(trifluoromethylsulfonyl)-imide (99.9%, Sigma-Aldrich), DHIICl (Bide Pharmatech), PEAI (Advanced Election Technology), (4-(7H-dibenzo[*c*,*g*]carbazol-7-yl)butyl)phosphonic acid (TCI), lead bromide (99.99%, Xi'an Yuri Solar), phenyl-C_{61}-butyricacidmethylester ($PC_{61}BM$; 99.5%, Advanced Election Technology), 2,9-dimethyl-4,7-diphenyl-1,10-phenanthroline (BCP, 96%, TCI), piperazinium iodide (99.5%, Xi'an Yuri Solar) and NiO_x nanoparticles (Advanced Election Technology). FAI, MACl, MABr, ThMAI, ThPyI and DHIII were synthesized using methods reported in the literature[35,36,45].

Substrate preparation

A fluorine-doped tin oxide (FTO) substrate (purchased from Advanced Election Technology) was washed sequentially with distilled water, acetone and isopropanol. Before use, the FTO was cleaned with ultraviolet–ozone for 20 min.

Preparation of bottom charge transport layers

For the n–i–p device. The SnO_2 electron transport layer (2.5 wt%, diluted by water) was coated on the substrate and annealed in air at 150 °C for 30 min. After cooling to room temperature, the substrate was treated with ultraviolet–ozone for 10 min before spin coating the perovskite solution.

For the p–i–n device. NiO_x nanocrystal (20 mg ml^{-1} in water) layers were first spin coated onto FTO at 5,000 rpm for 30 s and annealed on a hotplate at 150 °C for 15 min in air. After cooling, the substrates were immediately transferred to the nitrogen-filled glovebox. Then, 40 µl of 0.5 mg ml^{-1} of (4-(7H-dibenzo[*c*,*g*]carbazol-7-yl)butyl)phosphonic acid was dropped onto the NiO_x substrate spinning at 5,000 rpm for 20 s and this was post-annealed at 100 °C for 10 min.

Preparation of perovskite films

Perovskite films for two-step-processed n–i–p device. Here 1.5 M of PbI_2 with 2 mol% of CsI was dissolved in DMF:DMSO (v/v, 94/6) and then stirred at 70 °C for 3 h. The PbI_2 solution was then deposited by spin coating at 1,500 rpm for 30 s, dried at 70 °C for 1 min and then cooled to room temperature. For the control group, a solution of FAI/MACl (90:16 mg ml^{-1}) in IPA was spin coated on top of the PbI_2 layer at a rotation speed of 2,000 rpm for 35 s. For the DHIII- or ThPyI-based group with the buried 2D perovskite, a solution of FAI/MACl/DHIII or ThPyI (90/16/2 mg ml^{-1})/IPA was spin coated on the PbI_2 film followed by thermal annealing in air (relative humidity, ~50%–65%) at 120 °C for 20 min. After perovskite formation, the samples were transferred to a nitrogen-filled glovebox for further processing.

Perovskite films for one-step-processed n–i–p device. Here 1.55 M of nominal PbI_2, 1.4 M of FAI, 0.05 M of MAI, 0.05 M of CsI and 0.48 M of MACl in DMF:DMSO (8:1 volume) was prepared as the control solutions, and DHIII (2 mg ml^{-1}) was added to the control solutions as the target solutions. Then, 100 µl of the perovskite solution was spread on the substrate and spun using a one-step spin-coating process (3,500 rpm for 35 s at 5-s acceleration). Thereafter, 10–13 s before the end of the program, 300 µl of anisole as the anti-solvent was dripped on the film. The films were then annealed at 120 °C for 20 min.

Perovskite films for one-step-processed p–i–n device. Here 1.65 M of $FA_{0.85}MA_{0.1}Cs_{0.05}PbI_3$ perovskite solution with and without 2 mg ml^{-1} of DHIII was formulated by mixing CsI, FAI, MAI and PbI_2 with the corresponding stoichiometry ratio dissolved in a mixed solvent of DMF and DMSO with a volume ratio of 4:1. In addition, 10–20 mol% MACl and 5% excess PbI_2 were added to regulate the crystallization process. The 50-µl perovskite solution was dropped onto the substrate and this was followed by a two-step spin-coating procedure: 1,000 rpm for 5 s and 5,000 rpm for 30 s. Then, 150 µl of CB was dropped into the wet film for 10 s before the end of the procedure. Then, the as-deposited film was annealed at 110 °C for 20 min.

Perovskite films for two-step-processed wide-bandgap device (~1.70 eV, n–i–p type). Here 1.2 M of PbI_2 with 0.3 M of lead bromide and 0.33 M of CsI was dissolved in DMF:DMSO (v/v, 4/1) and then stirred at 60 °C for 2 h. The PbI_2 solution was then deposited by spin coating at 1,500 rpm for 30 s. For the control group, a solution of FAI/MABr/MACl (74/16/16 mg ml^{-1}) in IPA was spin coated on top of the PbI_2 layer at a rotation speed of 2,000 rpm for 35 s. For the DHIII-based group with the buried 2D perovskite, a solution of FAI/MABr/MACl/DHIII (90/16/16/2 mg ml^{-1}) was spin coated on the PbI_2 film followed by thermal annealing in air at 120 °C for 20 min. After perovskite formation, the samples were transferred to a nitrogen-filled glovebox for further processing.

Completion of device stack

For the n–i–p device. For the passivation layer, the ThPyBr solution was dissolved in 4 mg ml^{-1} of IPA and spin coated onto the perovskite surface at a spin rate of 5,000 rpm without any further processing. Then, the Spiro-OMeTAD solution (80 mg of Spiro-OMeTAD, 30 µl of 4-*tert*-butylpyridine and 17 µl of lithium bis(trifluoromethylsulfonyl)-imide (520 mg ml^{-1} in acetonitrile) in 1 ml of CB) was spin coated on the perovskite layer with 3,000 rpm for 30 s. Finally, an 18-nm MoO_3 layer and 100-nm Ag layer were deposited by thermal evaporation under a pressure of 1.0×10^{-4} Pa.

For the p–i–n device. Surface passivation was achieved by dripping 40 ml of piperazinium iodide solution (0.5 mg ml^{-1} in IPA) followed by spin coating at 4,000 rpm for 30 s and heating at 100 °C for 5 min. Subsequently, 20 mg ml^{-1} of $PC_{61}BM$ solution in CB was spin coated onto the perovskite films at 1,200 rpm for 20 s. Then, 0.6 mg ml^{-1} of BCP was spin coated on the $PC_{61}BM$ film at 1,000 rpm for 20 s. Finally, a 100-nm Ag electrode was deposited by thermal evaporation.

Growth of $(DHII)_2PbI_4$ crystals

The PbO powder (22.3 mg, 1.0 mmol) was dissolved in a mixture of 1.0 ml of aqueous HI and 0.2 ml of aqueous H_3PO_2 and stirred for 5–10 min at 120 °C. Then, 0.2 mmol of DHIII was added to the clear and bright yellow solution, which immediately produced orange crystals. The solution was heated and maintained at 120 °C until the crystals were fully dissolved. The solution was subsequently cooled down to room temperature without stirring. Plate crystals appeared at 50 °C. The crystals were filtrated, collected and transferred to a nitrogen-filled glovebox for further measurements.

Film characterization

SEM images were obtained using a ZEISS MERLIN Compact device at an accelerating voltage of 5 kV (commercially sourced FTO substrates (2.2 mm thickness) were unsuitable for cross-sectional SEM due to cutting limitations; ITO-coated glass (0.7 mm thickness) was substituted as the base for this analysis). X-ray diffraction measurements were carried out using a Rigaku Ultima IV X-ray powder diffractometer with Cu Kα radiation ($\lambda = 1.54$ Å) with a scan range from 3° to 50° at a scan rate of 20° min^{-1}. Optical absorption spectra of the perovskite films were obtained with a Cary 5000 ultraviolet–visible–near-infrared spectrophotometer. Steady-state

PL and TRPL measurements were performed by an FLS1000 PL spectrometer (Edinburgh Instruments) with excitation at 450 nm (~54 μW cm^{-2} for the PL measurement). TRPL was measured by excitation at 450 nm using an EPL 450-nm pulsed diode laser (pulse width, 79.4 ps; repetition rate, 0.1 MHz; maximum average power, 5 mW). All the PL and TRPL spectra (including Fig. 1e,f,i) were measured on glass/perovskite samples. For semi-in situ PL measurements during annealing, the perovskite films were deposited as wet films on a hotplate set to 80 °C for slow crystallization, allowing the monitoring of 2D phase formation. At 60-s intervals, the film was momentarily removed, flipped so that the glass side faced the excitation/detection optics and the PL spectrum was recorded through the glass. The sample was then immediately returned to the hotplate. All the PL measurements were performed with excitation through the glass side. X-ray photoelectron spectroscopy measurements and ultraviolet photoelectron spectroscopy measurements were performed using Thermo ESCALAB 250XI with perovskite films spin coated on the glass/ITO/SnO$_2$ substrates. Ultraviolet photoelectron spectroscopy measurements were performed using a He I excitation source (21.22 eV) under a base vacuum of 2×10^{-9} mbar with a pass energy of 2 eV. Confocal laser scanning fluorescence microscopy was measured by PicoQuant MicroTime 200, 440-nm picosecond pulsed diode laser (LDH440), pulse width of 70 ps, repetition frequency of 100 kHz and 20 μm × 20 μm test area.

GIWAXS patterns were obtained at the 1W1A Diffuse X-ray Scattering Station, Beijing Synchrotron Radiation Facility (BSRF-1W1A), using X-rays at a wavelength of 1.54792 Å. The diffraction angles were calibrated using NIST SRM660b (LaB6). For the in situ annealing experiments, the perovskite film was placed directly onto the heating stage of the GIWAXS instrument and, once secured, the radiation shield shutter was closed. Annealing was initiated by ramping the stage temperature from room temperature to the target set point at approximately 5 °C s^{-1}. GIWAXS patterns were continuously collected at 1-s intervals throughout the temperature ramp to monitor the phase evolution. On reaching the target temperature, the stage was held constant and the GIWAXS data were recorded during the isothermal hold to capture any subsequent crystal growth or phase transformations.

ToF-SIMS was conducted to evaluate the ion distributions in the perovskite film. The films were tested using a ToF-SIMS instrument (ION TOF-SIMS 5) with a Bi$^+$ primary beam (30 keV and 0.5 pA) and a Cs$^+$ sputter beam (0.5 keV and 30 nA). The sputter size was 300 μm × 300 μm, and the analysis size was 100 μm × 100 μm.

Device characterization

The J–V characteristics of the devices were measured using a Keithley 2400 source meter under standard AM1.5G illumination (Enli SS-F5-3A, Enli Technology), and the light intensity was calibrated using a standard silicon reference cell (Enli Technology). The calibrated report of the standard Si solar cell we used can be traced to NREL. The J–V curves were measured by forward scan (−0.1 to 1.22 V) and reverse scan (1.22 to −0.1 V) with a voltage step of 20 mV and a delay time of 20 ms. All the photovoltaic performance measurements were conducted using an aperture mask to accurately define the active area of the device. The aperture-masked area of the small-area and large-area devices were measured to be 0.0421 cm^2 and 1.007 cm^2, respectively. This measurement was performed using an optical microscope by a certified third-party institution (Tianjin Institute of Metrological Supervision and Testing). All the reported PCEs were determined based on this aperture-masked active area of 0.0421 cm^2 for small-area devices and 1.007 cm^2 for large-area devices. The external quantum efficiency curves of the encapsulated device were tested using a QE-R Solar Cell Spectral Response Measurement System (Enli Technology).

For the transient photovoltage decay and transient photocurrent decay measurements, a white light bias was generated from an array of diodes (Molex 180081-4320) with a light intensity about 0.5 sun. A diode-pumped laser (Lapa-80) was used as the perturbation source, with a pulse duration of 10 ns and a repetition frequency of 20 Hz. The perturbation light intensity was attenuated to keep the amplitude of transient V_{OC} below 10 mV so that $V_{OC} \ll V_{OC}$. Voltage and current dynamics were recorded on a digital oscilloscope (Tektronix MDO4104C), and voltages under open-circuit conditions and currents under short-circuit conditions were measured over a 1-MΩ and 50-Ω resistor, respectively.

The hole/ electron trap density and mobility of perovskite films were measured by the space-charge-limited-current method using a diode configuration of ITO/PEDOT:PSS/perovskite/Spiro-MeTAD/MoO$_3$/Ag for hole-only and ITO/SnO$_2$/perovskite/PCBM/BCP/Ag for electron-only devices. Dark I–V curves were collected in the range of 0–6 V with a 30-mV voltage step and a 2-ms delay time.

Data availability

All data are available in the article or its Supplementary Information. Additional information can be obtained from the corresponding authors upon reasonable request. The X-ray crystallographic coordinates for the structures reported in this study have been deposited at the Cambridge Crystallographic Data Centre (CCDC) under deposition numbers 2417858 and 2344072. These data can be obtained free of charge from the Cambridge Crystallographic Data Centre via www.ccdc.cam.ac.uk/data_request/cif. Source data are provided with this paper.

References

45. Lai, H. et al. Two-dimensional Ruddlesden-Popper perovskite with nanorod-like morphology for solar cells with efficiency exceeding 15. *J. Am. Chem. Soc.* **140**, 11639–11646 (2018).

Acknowledgements

Y.L. gratefully acknowledges financial support from the National Key Research and Development Program of China (grant number 2024YFB4205201) and the National Natural Science Foundation of China (grant numbers 22479121 and 52273182). We are thankful for the beam time provided by the 1W1A station (Beijing Synchrotron Radiation Facility) for GIWAXS characterization.

Author contributions

Y.G. and Y.L. conceived of the idea and designed the experiments. Y.G. carried out the fabrication, characterization and data collection of the perovskite films and devices. H.L. performed the density functional theory calculation of the organic spacers and supported the data analysis. Z.S. supported the device fabrication. Yu Chen supported the GIWAXS measurements. L.Y. and Z.H. contributed to the Kelvin probe force microscopy measurements. Y.Z. supported the visual representation of data. Y.G. wrote the first draft of the paper. Y.G. and Y.L. revised the paper. Yongsheng Chen and Y.L. supervised the whole project. All authors discussed the results and reviewed the paper.

Competing interests

The authors declare no competing interests.

Additional information

Supplementary information The online version contains supplementary material available at https://doi.org/10.1038/s41566-025-01797-9.

Correspondence and requests for materials should be addressed to Yongsheng Chen or Yongsheng Liu.

Peer review information *Nature Photonics* thanks Sang Il Seok, Christian Wolff and Zhigang Zang for their contribution to the peer review of this work.

Reprints and permissions information is available at www.nature.com/reprints.